SCIENCE CHINA Materials

ARTICLES

mater.scichina.com link.springer.com

Published online 30 May 2016 | doi: 10.1007/s40843-016-5057-8
Sci China Mater 2016, 59(5): 323–336

Hollow MO_x-RuO_2 (M = Co, Cu, Fe, Ni, CuNi) nanostructures as highly efficient electrodes for supercapacitors

Qiangqiang Tan[1], Pengfei Wang[1,2], Hui Liu[1,3], Yuxing Xu[1], Yunfa Chen[1] and Jun Yang[1,3*]

ABSTRACT Engineering the internal structure and chemical composition of nanomaterials in a cost-effective way has been challenging, especially for enhancing their performance for a given application. Herein, we report a general strategy to fabricate hollow nanostructures of ruthenium-based binary or ternary oxides via a galvanic replacement process together with a subsequent thermal treatment. In particular, the as-prepared NiO-RuO_2 hollow nanostructures loaded on carbon nanotubes (hNiO-RuO_2/CNT) with RuO_2 mass ratio at 19.6% for a supercapacitor adopting the KOH electrolyte exhibit high specific capacitances of 740 F g^{-1} at a constant current density of 1 A g^{-1} with good cycle stability. The specific capacitance for hNiO-RuO_2/CNT electrodes maintains 638.4 F g^{-1} at a current density of 5 A g^{-1}. This simple approach may shed some light on the way for making a wide range of metal oxides with tunable nanostructures and compositions for a variety of applications.

Keywords: ruthenium-based oxides, hollow nanostructures, galvanic replacement reaction, supercapacitor, specific capacitance

INTRODUCTION

A pesudocapacitor works based on the reversible Faradaic reactions (redox reactions) taking place on the electrode materials. However, chemical reactions are not 100% reversible even for the best combination of electrode materials and electrolyte. There are always some residual electrode materials that cannot participate in the reaction process, even after complete discharge. This is an unavoidable loss of active materials, which reduces the value of maximum specific capacitance with the increase of cycle numbers and affects the cycling stability of the pesudocapacitors. Despite the cyclic-stability issue, pesudocapacitors are still appealing due to their appropriate potential windows [1], higher energy density than that of conventional carbon materials, and better stability than conductive polymers [2–7].

Transition metal oxides are electrochemically active materials that facilitate redox reactions for charge build-up at the electrodes of pesudocapacitors [8–10]. Among various transition metal oxides as electrodes for supercapacitors, ruthenium dioxide (RuO_2) has been extensively studied because of its remarkably high theoretical specific capacitance, wide potential window, highly reversible redox reactions, good thermal stability, long cycle life, metallic-type conductivity, and high rate capability [11–14].

Increasing the specific surface areas and alloying/incorporating with other inexpensive transition metals are two effective ways to improve the performance of RuO_2 as electrode materials for supercapacitors. The former is capable for providing more active centers for the multiple redox reactions, which usually translates to the high specific capacitance, while the latter could not only significantly reduce the quantity of RuO_2 required in the electrode layer, favorable for the practical utilization of valuable ruthenium metals, but also improve the overall capacitive behavior by making use of the possible synergistic effect between different metal oxides. A number of strategies, such as depositing RuO_2 films on substrates with a rough surface [15–17], coating a thin RuO_2 film on high-surface-area materials [18,19], making nanometer-sized oxide electrodes [20,21], and decorating RuO_2 particles with transition metal oxides [22–26], have been explored to maximize the surface area

[1] State Key Laboratory of Multiphase Complex Systems, Institute of Process Engineering, Chinese Academy of Sciences, Beijing 100190, China
[2] University of Chinese Academy of Sciences, Beijing 100049, China
[3] Center for Mesoscience, Institute of Process Engineering, Chinese Academy of Sciences, Beijing 100190, China
* Corresponding author (email: jyang@ipe.ac.cn)

of RuO_2, and reduce the Ru usage. Unfortunately, despite these intriguing achievements, a number of challenges remain to be addressed before the RuO_2 can be commercially used as electrode materials for a supercapacitor. Typically, the surface area is usually difficult to tailor, and the strain developed in the RuO_2 during the charge/discharge processes often causes the cracking of the electrode, leading to poor long-term stability [27,28].

In this work, a general approach based on the combination of the galvanic replacement process with a subsequent thermal treatment was developed to generate carbon (C) or carbon nanotube (CNT)-supported hollow nanostructures of ruthenium-based binary or ternary oxides, labeled as hMO_x-RuO_2/C or hMO_x-RuO_2/CNT, as highly efficient electrodes for supercapacitors. In this strategy, transition metal nanoparticles (TMNPs) including Co, Cu, Fe, Ni, or CuNi were first prepared in an organic solvent, and they were then used as seeds in a galvanic replacement process to react with Ru ion precursors for the preparation of binary or ternary M-Ru nanoparticles with hollow interiors (hM-RuNPs). Subsequently, the as-prepared binary or ternary hM-RuNPs were loaded on the C or CNT supports and heated at elevated temperature under air to convert the metals into metal oxides for the generation of hMO_x-RuO_2/C or hMO_x-RuO_2/CNT electrode materials. Advantageously, the hollow interiors not only provide a large electrochemical active surface area for fast and reversible Faradaic reactions, but also facilitate the proton transport in the MO_x-RuO_2 shell by shortening the diffusion distance, while the carbon or carbon nanotube supports serve as an excellent conductor for fast electron transfer, and is helpful to maintain the high surface area of binary or ternary metal oxide nanoparticles by preventing them from aggregation. As a result of this unique structure, the final hMO_x-RuO_2/C or hMO_x-RuO_2/CNT exhibits improved performance as electrode materials for supercapacitors using KOH as electrolyte. In addition, the hollow interior may benefit the long-term stability of the metal oxide nanoparticles by relieving the strain effect developed during the charge-discharge process.

MATERIALS AND METHODS

General materials

The chemical reagents, including ruthenium(III) chloride ($RuCl_3$, Ru content 45–55%), cupper(II) acetylacetonate ($Cu(acac)_2$, 97.5%), nickel(II) acetylacetonate ($Ni(acac)_2$, 97.5%), cobalt(II) acetylacetonate ($Co(acac)_2$, 97.5%) and iron(III) acetylacetonate ($Fe(acac)_3$, 97.5%) and oleylamine (70%, technical grade) from Sigma-Aldrich, potassium hydroxide (KOH, 99%), ethanol (99.5%), methanol (99%), and toluene (99.5%) from Beijing Chemical Works, stainless steel gauze (200 mesh woven from 0.05 mm diameter wire) and commercial ruthenium(IV) oxide hydrate ($RuO_2{\cdot}xH_2O$, 54% Ru) with product number of 346088 from J&K Scientific Ltd., Vulcan XC-72 carbon powders with a BET surface area of 250 $m^2\ g^{-1}$ and an average particle size of 40–50 nm (XC-72C) from Cabot Corporation, carbon black with a BET surface area of 62 $m^2\ g^{-1}$ (SUPER C65) from Swiss Timcal Ltd., and polytetrafluoroethylene (PTFE, 60 wt.% aqueous dispersion) and multi-walled carbon nanotubes (CYL2-60) with a diameter of 40–60 nm, a length of 1–2 μm and a specific surface area of 100–150 $m^2\ g^{-1}$ from Shanghai Aladdin Bio-Chem Technology Co., Ltd., were used as received. Deionized water was produced by a Milli-Q Ultrapure-water purification system. All glassware and Teflon-coated magnetic stir bars were cleaned with aqua regia, followed by copious washing with de-ionized water before drying in an oven.

Synthesis of the transition metal (Co, Cu, Fe, Ni, CuNi) nanoparticles

In a typical synthesis of a monometallic or bimetalic transition metal nanoparticles, 102.8 mg of $Ni(acac)_2$, 104.7 mg of $Cu(acac)_2$, 102.9 mg of $Co(acac)_2$, 141.3 mg of $Fe(acac)_3$, or a mixture consisting of 51.4 mg of $Ni(acac)_2$ and 52.4 mg of $Cu(acac)_2$ was added to 20 mL of oleylamine in a three-necked flask fitted with a condenser and a stir bar. The solution was heated and kept at target temperature (160°C for Ni, Co and Fe, 190°C for Cu, and 190°C for CuNi) under flowing N_2 for 2 h for the reduction of transition metal ions by oleylamine. After reaction, the monometallic or bimetallic transition metal nanoparticles were purified by precipitation with methanol, centrifugation, washing with methanol, and re-dispersed in 20 mL of toluene.

Synthesis of the hollow structured M–Ru nanoparticles

Typically, 104.7 mg of $Ni(acac)_2$, 102.8 mg of $Cu(acac)_2$, 102.9 mg of $Co(acac)_2$, 141.3 mg of $Fe(acac)_3$, or a mixture consisting of 51.4 mg of $Ni(acac)_2$ and 52.4 mg of $Cu(acac)_2$ was added to 20 mL of oleylamine in a three-necked flask fitted with a condenser and a stir bar. The solution was heated and kept at target temperature (160°C for Ni, Co and Fe, 190°C for Cu, and 190°C for CuNi) under flowing N_2 for 2 h for the reduction of transition metal ions. Then 40.7 mg of $RuCl_3$ was added swiftly, followed by increasing the temperature to 240°C and keeping at the temperature for 2 h for

the completion of the replacement reaction between transition metal nanoparticles and Ru ion precursors. After reaction, the as-obtained binary or ternary M-Ru nanoparticles with hollow interiors, labeled as hM-RuNPs, were purified by precipitation with methanol, centrifugation, washing with methanol, and re-dispersed in 20 mL of toluene.

Loading the hM-RuNPs on carbon or carbon nanotube supports

For the loading of the hM-RuNPs on the Vulcan XC-72 carbon or CYL2-60 carbon nanotube supports, 30 mg of carbon powder or CNT was added to the toluene solution of hM-RuNPs. After stirring the mixture for 24 h, the hM-RuNPs supported on C or CNT labeled as hM-Ru/C or hM-Ru/CNT were collected by centrifugation, washed thrice with ethanol, and then dried at room temperature in vacuum.

Synthesis of the hMO_x–RuO_2/C or hMO_x–RuO_2/CNT

The hM-Ru/C and hM-Ru/CNT as-prepared above were heated at 350°C in air for 6 h to convert the transition metals and Ru into their oxide states (MO_x and RuO_2) for the generation of the final hMO_x-RuO_2/C or hMO_x-RuO_2/CNT electrode materials.

Particle characterizations

Transmission electron microscopy (TEM), high-resolution TEM (HRTEM) and scanning TEM (STEM) were performed on the JEOL JEM-2100 and FEI Tecnai G^2 F20 electron microscope operating at 200 kV with supplied software for automated electron tomography. For the TEM measurements, a drop of the particle solution was dispensed onto a 3-mm carbon-coated copper grid (or molybdenum grid for the samples containing copper). Excessive solution was removed by an absorbent paper, and the sample was dried under vacuum at room temperature. An energy dispersive X-ray spectroscopy (EDX) analyzer attached to the TEM was used to determine the element distributions in the hollow structured nanoparticles. The mean particle size, the average thickness of the shells, and the standard deviations were calculated from a few randomly chosen areas in the TEM image containing approximately 100 nanoparticles each. The metal contents were measured using inductively coupled plasma atomic emission spectrophotometry (ICP-AES, Optima 5300DV, Perkin Elmer). X-ray photoelectron spectroscopy (XPS) was conducted on a VG ESCALAB MKII spectrometer. Powder X-ray diffraction (XRD) patterns were recorded on a Rigaku D/Max-3B diffractometer, using Cu Kα radiation (λ=1.54056 Å). Samples for XPS and XRD analyses were concentrated from the toluene solution of nanoparticles to 0.5 mL using flowing N_2. Ten milliliters of methanol was then added to precipitate the nanoparticles, which were recovered by centrifugation, washed with methanol, and then dried at room temperature in vacuum.

Fabrication of the electrode and the electrochemical measurements

The working electrodes were fabricated by mixing the as-prepared hollow oxides (hCoO-RuO_2/C, hCoO-RuO_2/CNT, hCuO-RuO_2/C, hCuO-RuO_2/CNT, hFe_2O_3-RuO_2/C, hFe_2O_3-RuO_2/CNT, hNiO-RuO_2/C, hNiO-RuO_2/CNT, hCuNiO-RuO_2/C, or hCuNiO-RuO_2/CNT) or commercial RuO_2, carbon black, and polytetrafluoroethylene (PTFE) with a mass ratio of 85/10/5. The mixture was dispersed in small amount of ethanol for the formation of paste, and was then pressed into slices and dried at 100°C for 10 h in vacuum. Subsequently, the slices were coated onto the stainless steel gauzes under the pressure of 10 MPa to obtain the electrode. The mass of as-prepared hMO_x-RuO_2/C or hMO_x-RuO_2/CNT coated on the stainless steel gauze was 4.0 mg.

All of the electrochemical measurements were carried out using a two electrode setup: the stainless steel gauzes that coated with hMO_x-RuO_2/C or hMO_x-RuO_2/CNT was used as the working electrode, and the coin-cells (20 mm in diameter and 1.6 mm in thickness) fabricated with polypropylene membrane (purchased from NKK, 45 μm in thickness) were used as the separator. The cells were aged for 24 h before measurement. The measurements were performed in 6 mol L^{-1} aqueous KOH electrolyte at room temperature. Cyclic voltammetry (CV), galvanostatic charge–discharge test, and electrochemical impedance spectroscopy (EIS) measurements were obtained using a CHI650 electrochemical workstation. CV tests were done between 0 and 1.2 V at the scan rates of 20, 50, 100, and 200 mV s^{-1}. Charge–discharge cycling tests at a constant current mode between 0 and 1 V and the rate capability at current densities of 0.5, 1, 2, 5 A g^{-1} were performed on a computer controlled Land battery tester. EIS measurements were conducted over the frequency range from 100 kHz to 10 mHz. The specific capacitance of the electrode can be calculated using the following equation:

$$C = It / \Delta Vm, \quad (1)$$

where C is the specific capacitance (F g^{-1}), I is the response current density (A g^{-1}), t is the discharge time (s), ΔV is the potential (V), and m is the mass of the electroactive

materials in the electrodes (g).

RESULTS AND DISCUSSION

Fig. 1 schematically shows the overall strategy for the formation of hMO_x-RuO_2/C or hMO_x-RuO_2/CNT electrode materials. Monometallic or bimetallic TMNPs were firstly synthesized by reducing their single or mixed acetylacetonate precursors in oleylamine, which serves as solvent, capping surfactant and reducing agent [29–31]. The TMNPs thus obtained were then used as seeds for the subsequent replacement reaction with ruthenium (Ru) ions. The TEM and HRTEM images of the TMNPs as-prepared in oleylamine are shown in Fig. S1 (Supplementary information (SI)). As displayed, these TMNPs are quasi-spherical, nearly dispersed, and have an average diameter of ca. 20.8 nm for Co, 29.8 nm for Cu, 16.2 nm for Fe, 31.6 nm for Ni, and 40.6 nm for CuNi, respectively. The successful preparation of the TMNPs was confirmed by heir XPS analyses (Fig. S2). The 2p spectra of all the TMNPs can be de-convoluted into two pairs of doublets. The more intense doublet (at 778.5 and 794.6 eV for Co, 933.1 and 952.8 eV for Cu, 707.0 and 720.1 eV for Fe, 852.8 and 870.1 eV for Ni, 932.0 and 951.8 eV for Cu in bimetallic CuNi, and 853.4 and 870.6 eV for Ni in bimetallic CuNi, respectively) corresponds to the transition metals at zero valent state, while the second and weaker doublet, with binding energies higher than those of zero valent transition metals could be assigned to Co, Cu, Fe, and Ni at oxidized state, e.g., CoO, CuO, Fe_2O_3, and NiO [32,33]. In addition, for Co, Cu and Ni, the satellite peaks in their XPS spectra are also observed [34,35].

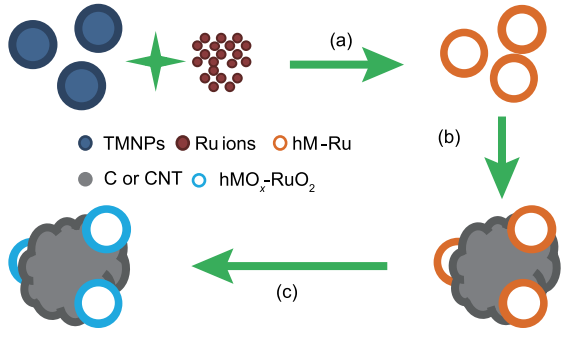

Figure 1 Schematic illustration showing the formation of hMO_x-RuO_2/C or hMO_x-RuO_2/CNT electrode materials: (a) hM-RuNPs were firstly prepared via galvanic replacement between TMNPs and Ru ion precursors, (b) the as-prepared hM-RuNPs were loaded on carbon or carbon nanotube supports, and then (c) the hM-RuNPs were converted into hMO_x-RuO_2 particles on the carbon or carbon nanotube supports via thermal treatment.

As displayed in Fig. 1, in the strategy developed in this work, the preparation of binary or ternary hM-RuNPs is an important step preceding the fabrication of hMO_x-RuO_2/C or hMO_x-RuO_2/CNT electrode materials. The binary or ternary hM-RuNPs were synthesized using a seed-mediated growth method at elevated temperature. The replacement reaction between TMNPs and the Ru ion precursors in oleylamine can be described as $3M + xRu^{3+} \rightarrow xRu + 3M^{x+}$, where M means transition metals at zero valent state. Pure TMNPs are transformed into alloy shells composed of corresponding transition metal and Ru by galvanic replacement [36–38]. Actually, the real process occurred in the solution is more complicated. In addition to the replacement reaction between TMNPs and Ru precursors, it also involves the oleylamine reduction of transition metal ions generated from galvanic replacement, the reduction of Ru ions added to the solution, and perhaps the alloying between Ru and transition metal atoms. Overall, these closely knitted reactions collectively facilitate the formation of binary or ternary nanoshells consisting of Ru and corresponding transition metals.

The typical TEM and HRTEM images of the as-prepared hM-RuNPs are shown in Figs $2a_1$–e_1 and $2a_2$–e_2, respectively, in which the hollow interiors could be clearly discerned by the strong brightness contrast between central and surface regions. These binary and ternary hM-RuNPs have an average size of ca. 14.2 nm for hCo-RuNPs, 18.6 nm for hCu-RuNPs, 16.4 nm for hFe-RuNPs, 23.8 nm for hNi-RuNPs, and 34.4 nm for hCuNi-RuNPs, respectively. Except for the hFe-RuNPs, which remain same size as their Fe seeds, the as-prepared hM-RuNPs are smaller in diameter in comparison with their corresponding transition metal seed particles. The alloy nature in the shells of the binary and ternary hM-RuNPs could be confirmed by the distributions of transition metals and Ru in the binary and ternary hM-RuNPs, which were analyzed by EDX under the high-angle annular dark-field scanning TEM (HAADF-STEM) mode. As demonstrated by Figs $2a_3$–a_6 for hCo-RuNPs, $2b_3$–b_6 for hCu-RuNPs, $2c_3$–c_6 for hFe-RuNPs, $2d_3$–d_6 for hNi-RuNPs, and $2e_3$–e_7 for hCuNi-RuNPs, respectively, the nanoscale elemental mappings reveal that the corresponding transition metals and Ru are distributed uniformly in the shell regions. The elemental mapping assays are well in accord with the line scanning analyses of a number of hM-RuNPs in the HAADF-STEM mode (Figs $2a_7$ for hCo-RuNPs, $2b_7$ for hCu-RuNPs, $2c_7$ for hFe-RuNPs, $2d_7$ for hNi-RuNPs, and $2e_8$ for hCuNi-RuNPs, respectively), which also show the uniform distribution of the corresponding transition

metals and Ru throughout the shells of hM-RuNPs. The average thickness of the shells and their standard deviations, which are calculated directly from the TEM images, are 1.6 nm and 0.31 nm for hCo-RuNPs, 1.3 nm and 0.22 nm for hCu-RuNPs, 1.5 nm and 0.41 nm for hFe-RuNPs, 2.2 nm and 0.55 nm for hNi-RuNPs, and 3.4 nm and 0.98 nm for hCuNi-RuNPs, respectively. Furthermore, the HRTEM images (Figs 2a_2–e_2) not only indicate the presence of

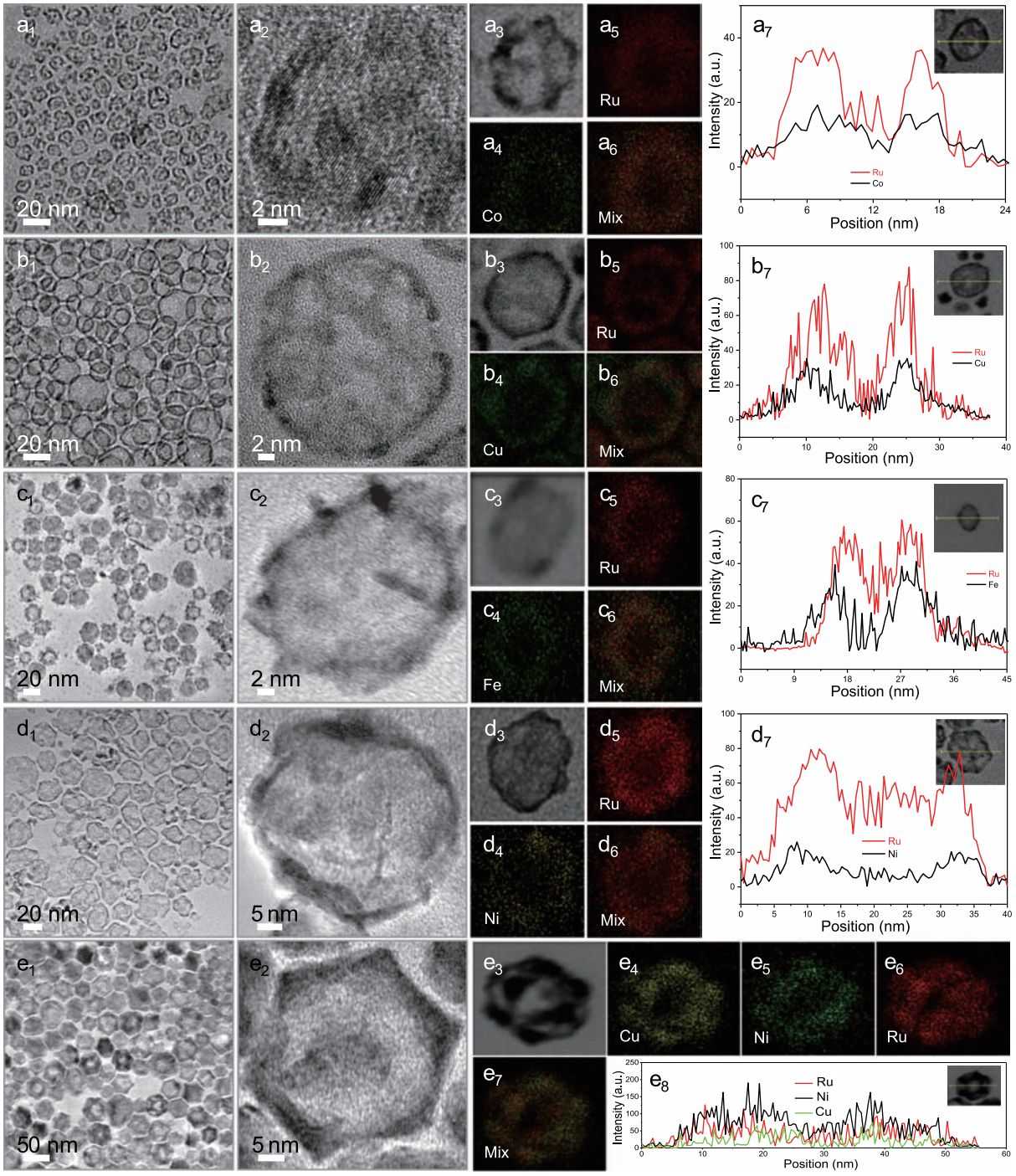

Figure 2 TEM images (a_1–e_1), HRTEM images (a_2–e_2), elemental mapping analyses (a_3–a_6, b_3–b_6, c_3–c_6, d_3–d_6, e_3–e_7), and element profiles (a_7–d_7, e_8) of binary Co-Ru (a_1–a_7), Cu-Ru (b_1–b_7), Fe-Ru (c_1–c_7), Ni-Ru (d_1–d_7), and ternary CuNi-Ru hollow structured nanoparticles (e_1–e_8) synthesized in oleylamine via galvanic replacement between TMNPs and Ru ion precursors.

hollow interiors in the hM-RuNPs, but also reveal the additional structural details. The discontinuous feature of the alloy shell could be clearly identified. The formation of the discontinuous alloy shells is important, as it permits the access of the inner surfaces for the occurrence of multiple redox reactions.

After aging the mixture of hM-RuNPs in toluene and carbon or carbon nanotube for 24 h at room temperature, the nanoparticles could be efficiently loaded on the carbon or carbon nanotube supports, leaving behind a clear toluene phase. The representative TEM images (Figs 3a, e, i, m, and q for carbon- and Figs 3c, g, k, o, and s for carbon nanotube-

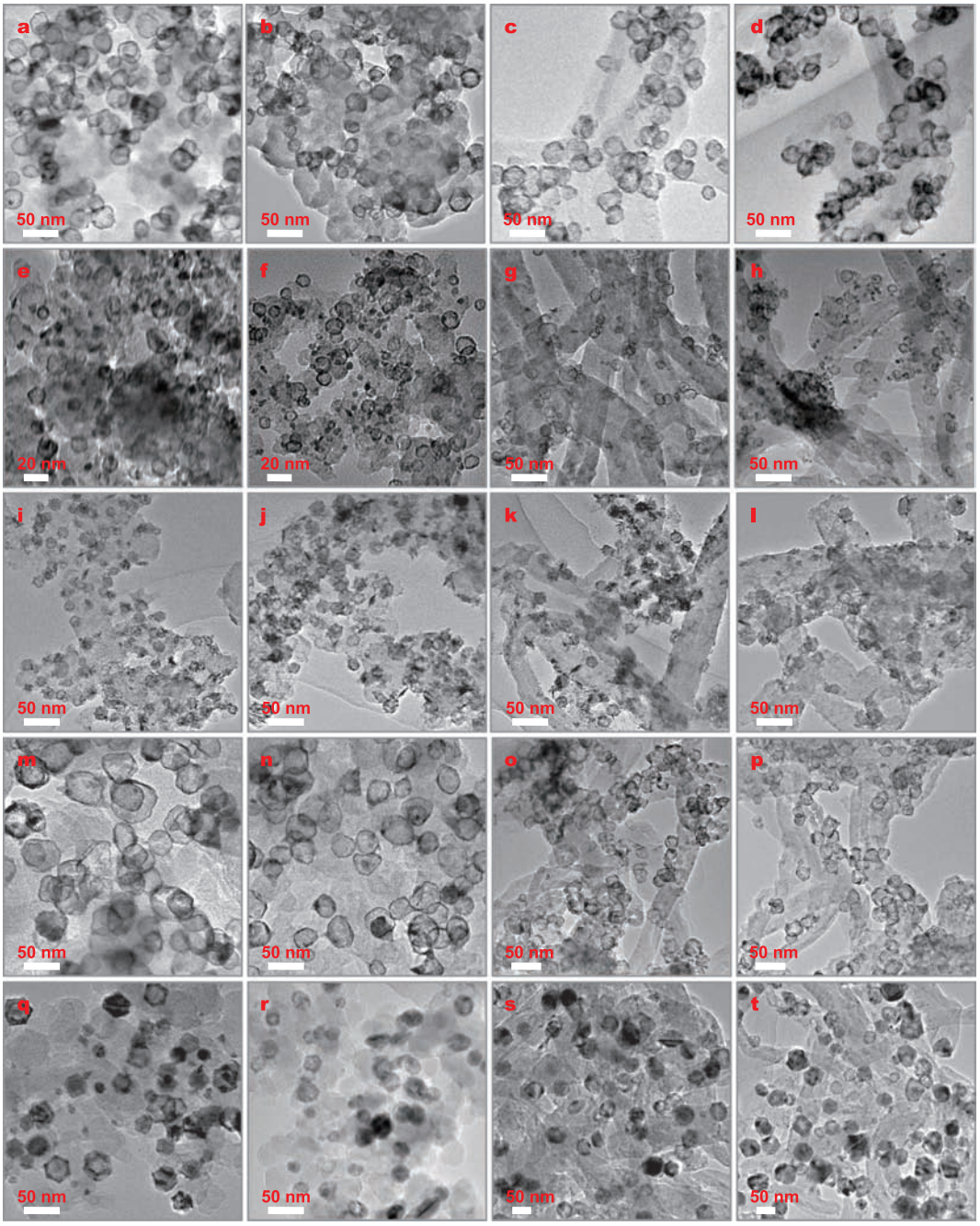

Figure 3 TEM images of the as-prepared hCo-Ru (a, c), hCoO-RuO_2 (b, d), hCu-Ru (e, g), hCuO-RuO_2 (f, h), hFe-Ru (i, k), hFe$_2$O$_3$-RuO_2 (j, l), hNi-Ru (m, o), hNiO-RuO_2 (n, p), hCuNi-Ru (q, s), and h$Cu_{0.6}Ni_{0.4}$O-RuO_2 (r, t) supported on carbon (a, b, e, f, i, j, m, n, q, r) and carbon nanotubes (c, d, g, h, k, l, o, p, s, t).

supported hCo-Ru, hCu-Ru, hFe-Ru, hNi-Ru, and hCuNi-Ru, respectively) show that the binary and ternary hM-RuNPs are dispersed very well on the carbon or carbon nanotube supports. Subsequently, the hM-Ru/C and hM-Ru/CNT were subjected to calcination at 350°C in air for 6 h to convert the transition metals and Ru in the nanoshells into their oxidized states for the generation of final hMO_x-RuO_2/C or hMO_x-RuO_2/CNT electrode materials.

We employed carbon-supported hM-RuNPs as the typical examples to carry out the XPS examinations, which were used to determine the chemical states of the transition metals and Ru before and after calcination. The XPS results of Ru in hM-RuNPs before and after calcination are shown in Fig. 4. Because the Ru $3d_{3/2}$ peak overlaps with the C 1s peak in XPS spectra, preventing an unambiguous analysis of the nanoparticle surface, the Ru 3p XPS peak is used instead. As shown in Figs 4a, c, e, g, and i for the XPS spectra of the Ru in hCo-Ru, hCu-Ru, hFe-Ru, hNi-Ru, and hCuNi-Ru before calcination, the doublets at 461.9–462.5 eV and 484.2–484.8 eV are signatures of Ru metal in the zero valent state [32]. However, after calcination in air, the doublets at 463.6–463.9 eV and 486.1–486.4 eV for the Ru in hM-RuNPs, which reflect the Ru at oxidized state, e.g., RuO_2 [32,39–41], can fit for the XPS spectra very well (Figs 4b, d, f, h, and j for the XPS spectra of the Ru in hCo-Ru, hCu-Ru, hFe-Ru, hNi-Ru, and hCuNi-Ru after calcination), indicating that the complete conversion from Ru to RuO_2 has been achieved upon the thermal treatment of hM-RuNPs in air at elevated temperature. The XPS spectra of the corresponding transition metals in hM-RuNPs before and after calcination are shown in Fig. S3. As displayed, all transition metals have been partially oxidized before calcination because they are susceptible to oxidation (Figs S3a, c, e, g, i, and l for Co in hCo-Ru, Cu in hCu-Ru, Fe in hFe-Ru, Ni in hNi-Ru, Cu in hCuNi-Ru, and Ni in hCuNi-Ru, respectively). However, after calcination, the XPS peaks associated with the zero valent state disappeared, as exhibited in Figs S3b, d, f, h, j, and m for Co in hCo-Ru, Cu in hCu-Ru, Fe in hFe-Ru, Ni in hNi-Ru, Cu in

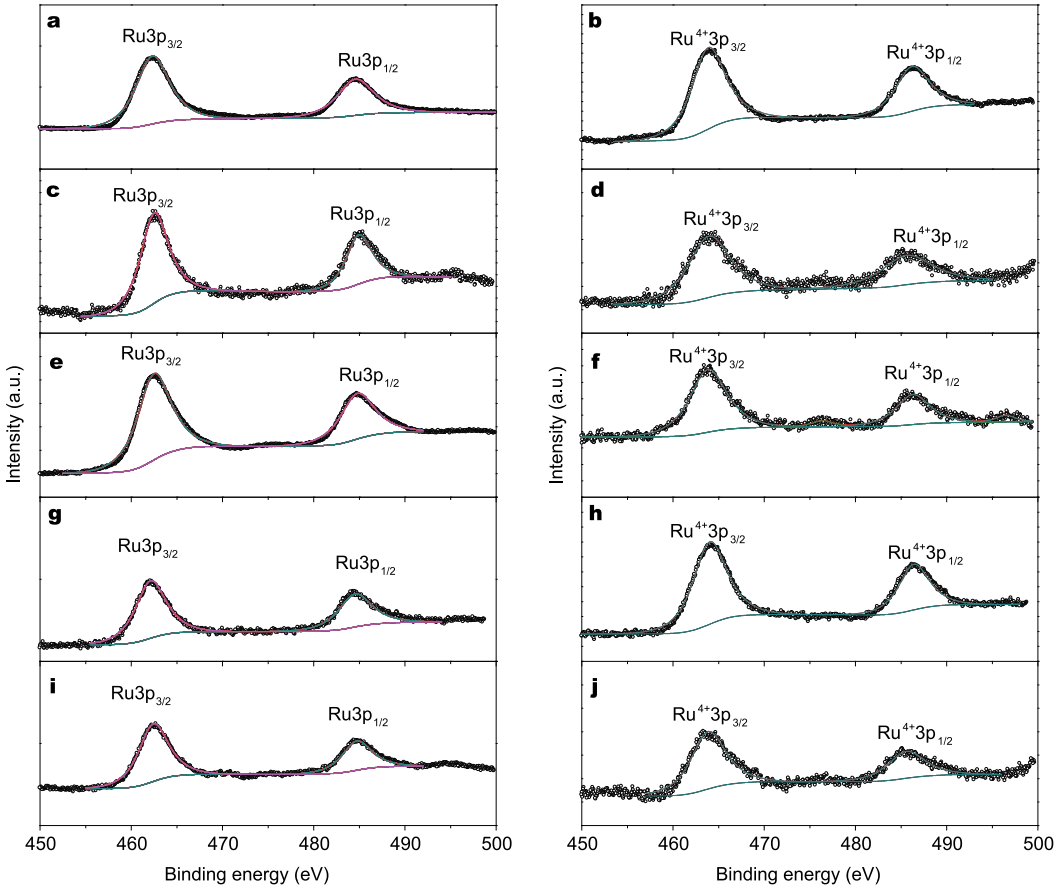

Figure 4 XPS spectra of the Ru in hCo-Ru (a, b), hCu-Ru (c, d), hFe-Ru (e, f), hNi-Ru (g, h), and hCuNi-Ru (i, j) before (a, c, e, g, i) and after calcination in air (b, d, f, h, j), respectively.

hCuNi-Ru, and Ni in hCuNi-Ru, respectively, suggest the successful conversion for the transition metals from zero valent metal to metal oxides, e.g., CoO, CuO, Fe_2O_3, and NiO [32,42].

In addition, the transformation for the transition metals and Ru from zero valent states to their oxidized states on the carbon or carbon nanotube supports could be further confirmed by XRD analyses. The XRD patterns of hM-Ru/C and hM-Ru/CNT before and after calcination in air are shown in Figs S4 and 5, respectively. As indicated, the homogeneously mixed crystal lattices, which indicate the formation of alloy nanoshells, in the XRD patterns for the hM-Ru/C and hM-Ru/CNT before calcination (a, c, e, g, and i in Figs S4 and 5 for hCo-Ru, hCu-Ru, hFe-Ru, hNi-Ru, and hCuNi-Ru, respectively) have been converted into mixed phases consisting of corresponding face-centered cubic (for CoO), monoclinic (for CuO), cubic (for Fe_2O_3), or hexagonal (for NiO) transition metal oxides and tetragonal RuO_2 after thermal treatment (b, d, f, h, and j in Figs S4 and 5 for hCo-Ru, hCu-Ru, hFe-Ru, hNi-Ru, and hCuNi-Ru, respectively).

The mass ratios of the transition metal oxides and RuO_2 in the final hMO_x-RuO_2/C and hMO_x-RuO_2/CNT were determined by ICP-AES, and the results were summarized in Table S1. As shown, the hCuO-RuO_2 and $hCu_{0.6}Ni_{0.4}O$ have lower contents of MO_x in comparison with those in other hollow nanostuructures. The complexity in the synthesis process, which involves the replacement reaction between TMNPs and Ru precursors, the oleylamine reduction of transition metal ions generated from galvanic replacement, the reduction of Ru ions added to the solution, and the alloying between Ru and transition metal atoms, may account for the different composition in the final hollow products. In specific, a molar ratio of 6/4 is obtained for the Cu and Ni in ternary $hCuNiO_x$-RuO_2/C or $hCuNiO_x$-RuO_2/CNT product, which is slightly higher than the Cu/Ni precursor ratio (1/1) used to produce bimetallic CuNi seed particles.

The TEM images of the final hMO_x-RuO_2/C and hMO_x-RuO_2/CNT products are also exhibited in Fig. 3 (b, f, j, n, and r for carbon- and d, h, l, p, and t for carbon nanotube-supported hCoO-RuO_2, hCuO-RuO_2, hFe_2O_3-RuO_2, hNiO-RuO_2, and $hCu_{0.6}Ni_{0.4}O$-RuO_2, respectively), which manifest that the resulting binary and ternary hMO_x-RuO_2 nanoparticles in the final products have the same size, size distribution, and hollow interiors as those of their hollow structured alloy precursors. In addition, the well dispersion of hMO_x-RuO_2 on the carbon or carbon nanotube supports is also maintained after calcination at elevated temperature in air.

The final hMO_x-RuO_2/C and hMO_x-RuO_2/CNT products were examined as electrode materials for a supercapacitor and benchmarked with the commercial $RuO_2{\cdot}xH_2O$ from J&K Scientific Ltd. The a and c series in Fig. 5 show the CVs of the as-prepared hMO_x-RuO_2 nanoparticles and commercial RuO_2 supported on carbon (Figs 5a_1, a_2, a_3, a_4, a_5, and a_6) and carbon nanotubes (Figs 5c_1, c_2, c_3, c_4, c_5, and c_6) obtained in 6 mol L^{-1} KOH with a potential range of 0–1.2 V at the scan rates of 20, 50, 100, and 200 mV s^{-1}, respectively. For the same mass loading, the CV loops have different areas for different electrode materials, indicating different levels of stored charge. In general, the metal oxides usually display redox reaction. However, the RuO_2 has multiple continuous redox peaks, which are overlaying together to show double-layer-like capacitor. Further, because of the different pseudocapacitance of MO_x, the hMO_x-RuO_2 hollow nanosturctures exhibit various redox features. In comparison with those of other hMO_x-RuO_2 and commercial RuO_2 samples, the CV curves of hCoO-RuO_2 (Figs 5a_1 and c_1) and hNiO-RuO_2 (Figs 5a_4 and c_4) supported on carbon (Figs 5a_1 and a_4) and carbon nanotubes (Figs 5c_1 and c_4) have obvious redox peaks, clearly illustrating their typical pseudocapactive mechanism. In specific, besides more rectangle shapes, which usually reveals perfect electrochemical reversibility of the Faradaic redox transitions on the surface of oxides, both hNiO-RuO_2/C and hNiO-RuO_2/CNT electrodes (Figs 5a_4 and c_4, respectively) exhibit much higher current densities than those of other carbon or carbon nanotube-supported hMO_x-RuO_2 and commercial RuO_2 samples, suggesting that they have higher electrochemical capacitance.

The specific capacitances calculated from the CV loops for the hMO_x-RuO_2/C, hMO_x-RuO_2/CNT, and commercial RuO_2 samples, which are summarized in Table S2, exhibit decreased trend with the increase of scan rates owing to the limited rate of ion diffusion at high scan rates. As evinced, the specific capacitances of most hMO_x-RuO_2 products are comparable with that of commercial RuO_2 samples, particularly at high scan rates, although the mass ratios of RuO_2 in these binary or ternary hollow structures are less than 40%. In particular, the specific capacitance value for the supercapacitors based on hNiO-RuO_2/CNT electrode can reach 947.1 F g^{-1} (based on total mass of metal oxides) at scan rate of 20 mV s^{-1}. This value is much higher than the recent data reported for RuO_2-based electrodes, e.g., 642 F g^{-1} for the mesoporous Co_3O_4/$RuO_2{\cdot}xH_2O$ composites [22], 162.4 F g^{-1} for the MnO_x-RuO_2 nanofiber mats [23], 173.2 F g^{-1} for the electro-spun RuO_2-Ag_2O composite

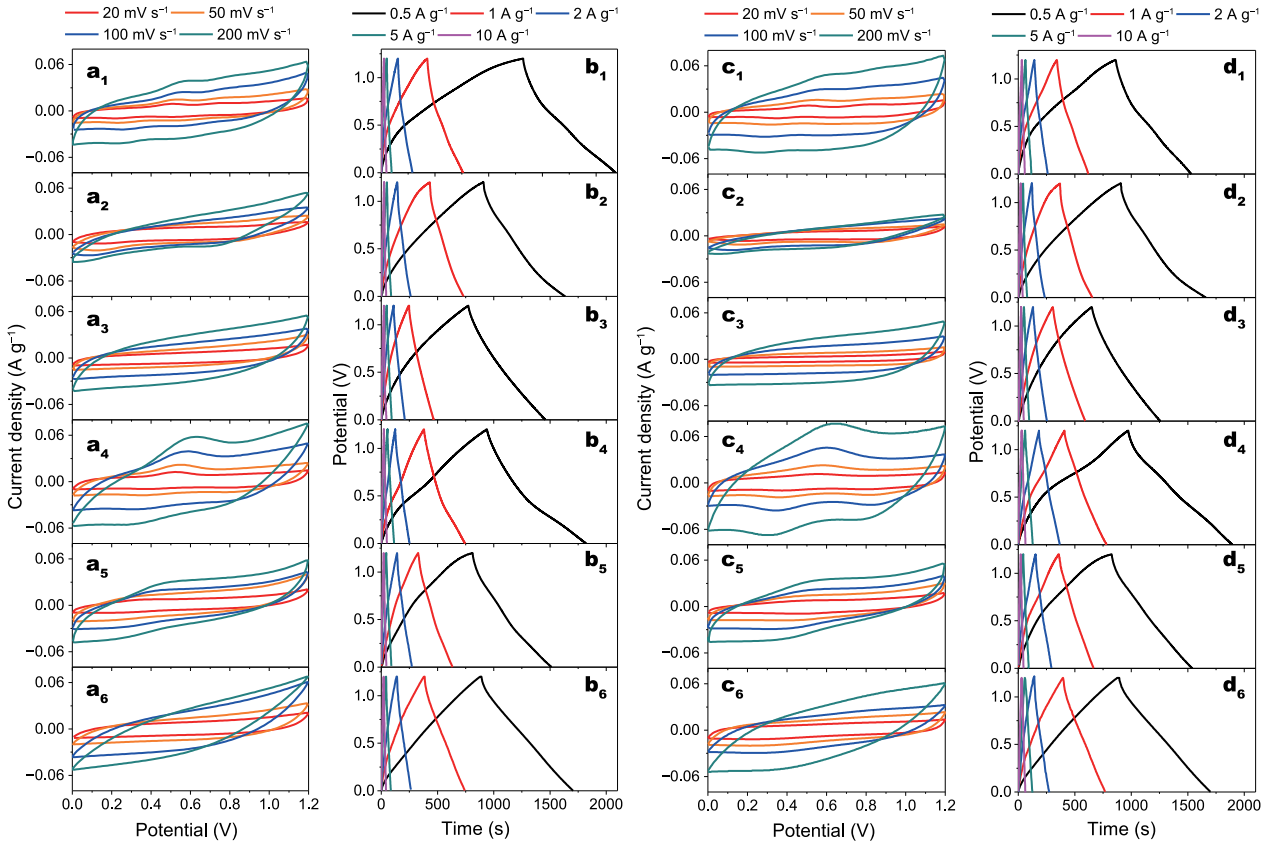

Figure 5 Cyclic voltammograms of hCoO-RuO_2 (a_1, c_1), hCuO-RuO_2 (a_2, c_2), hFe_2O_3-RuO_2 (a_3, c_3), hNiO-RuO_2 (a_4, c_4), h$Cu_{0.6}Ni_{0.4}O$-RuO_2 (a_5, c_5), and commercial RuO_2 (a_6, c_6) supported on carbon (a_1, a_2, a_3, a_4, a_5, a_6) and carbon nanotubes (c_1, c_2, c_3, c_4, c_5, c_6) at different scan rates; galvanostatic charge-discharge curves of hCoO-RuO_2 (b_1, d_1), hCuO-RuO_2 (b_2, d_2), hFe_2O_3-RuO_2 (b_3, d_3), hNiO-RuO_2 (b_4, d_4), h$Cu_{0.6}Ni_{0.4}O$-RuO_2 (b_5, d_5), and commercial RuO_2 (b_6, d_6) supported on carbon (b_1, b_2, b_3, b_4, b_5, b_6) and carbon nanotubes (d_1, d_2, d_3, d_4, d_5, d_6) at different current densities.

nanowires [24], 590 F g^{-1} for the Co_3O_4@RuO_2 nanosheet arrays on carbon cloth [25], 905 F g^{-1} for the RuO_2 nanoparticle decorated mesoporous Co_3O_4 nanosheet [26], 620 F g^{-1} for the Ru-Co mixed oxide deposited on single-walled carbon nanotubes [43], and 710 F g^{-1} for the SnO_2-RuO_2 composite films (based on pure RuO_2 not the total composite) [44]. Even at a high scan rate of 200 mV s^{-1}, the hNiO-RuO_2/CNT electrode still yields a high capacitance of 533.9 F g^{-1}. The better capacitive behavior of hMO_x-RuO_2/C and hMO_x-RuO_2/CNT products in comparison with that of other RuO_2-based electrodes and commercial RuO_2 might be attributed to the large surface area of the hollow structures, where the discontinuous shells allow the internal surface of the binary and ternary hMO_x-RuO_2 nanoparticles to be accessible for the multiple redox reactions. In addition, the relatively short diffusion distance for the ions in the thin shell of hMO_x-RuO_2 samples would also be helpful for enhancing the electro-active sites.

It is noteworthy that although carbon nanotubes usually have superior electronic conductivity, the binary or ternary hollow nanostructures supported on them do not always show higher specific capacitance than that of their counterparts supported on carbon powders. This is because in addition to the electronic conductivity of the supports, the specific capacitance is also associated with the interaction between active materials and substrates and the dispersity of the active materials on the surface of substrates.

To further identify the electrochemical performance of all carbon and carbon nanotube-supported hMO_x-RuO_2 products as electrodes for supercapacitors, the galvanostatic charge–discharge measurements were conducted at current densities of 0.5, 1, 2, 5, and 10 A g^{-1}. As shown in b and d of Fig. 5 for the galvanostatic charge–discharge curves of hMO_x-RuO_2 and commercial RuO_2 samples supported on carbon and carbon nanotubes, respectively, the almost triangular shapes at each current density indicate their good electrochemical reversibility within a stable potential window of 0–1.2 V because of the high degree of symmetry in charge and discharge. In specific, for the

hNiO-RuO_2/C (Fig. 5b$_4$) and hNiO-RuO_2/CNT samples (Fig. 5d$_4$), slight plateaus appearing during the charge–discharge process further verify their pseudo-capacitance behavior, which corresponds well with the CV curves.

Figs 6a and b show the specific capacitances of hMO_x-RuO_2 and commercial RuO_2 supported on carbon and carbon nanotubes at the current density of 0.5, 1, 2, and 5 A g^{-1}, respectively, which are calculated based on the total mass of oxides. The specific capacitances measured at different current densities for hMO_x-RuO_2 and commercial RuO_2 supported on carbon or carbon nanotubes are listed in Table S3. Again, the hNiO-RuO_2/C and hNiO-RuO_2/CNT exhibit higher capacitances at all current densities (758.8, 686.4, 625.8, 550.0 F g^{-1} for hNiO-RuO_2/C and 792.1, 740.0, 704.5, and 638.4 F g^{-1} for hNiO-RuO_2/CNT at current density of 0.5, 1, 2, and 5 A g^{-1}, respectively) than those of other hMO_x-RuO_2 as well as the commercial RuO_2 supported on the same substrates. The optimized microstructure in terms of nano-channels in the particle shell, shell thickness, and surface morphology, interaction and mass ratio between RuO_2 and transition metal oxide, and the distribution of the hollow oxides over the substrates may account for the superior specific capacitance for this sample.

The cycle life is another important factor for evaluating the performance of electrode materials for a supercapacitor. The comparison of the long-term cycling performance of the electrode materials at constant current density of 1 A g^{-1} is illustrated in Figs 6c and d for carbon and carbon nanotube as substrates, respectively. The specific capacitance retention ratios after 2000 cycles, which are calculated from Figs 6a and b, are presented in Table S4. As shown, except for hNiO-RuO_2/C and $hCu_{0.6}Ni_{0.4}O$-RuO_2/C, which have 88.2% and 85.6% retention of their ini-

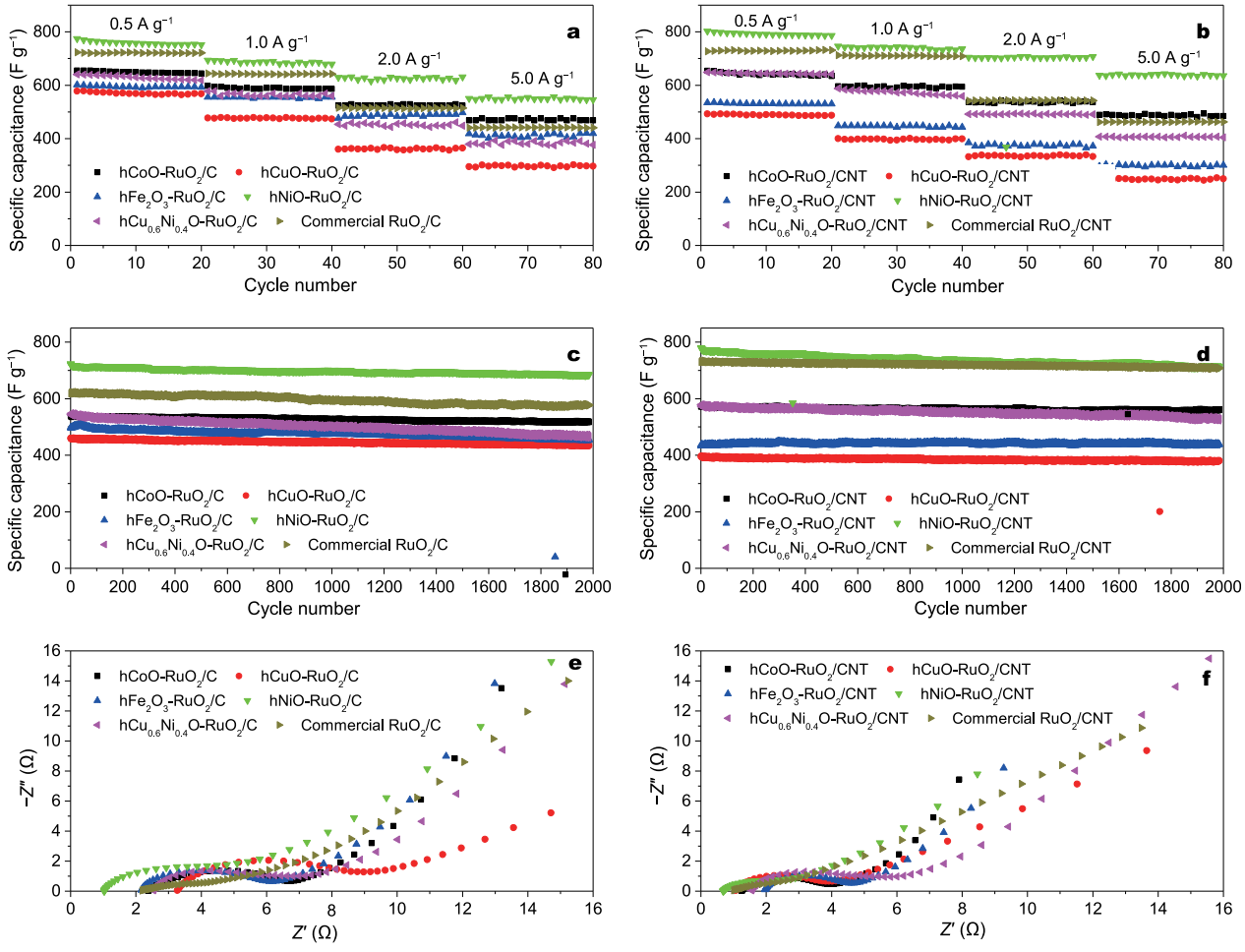

Figure 6 Plots of specific capacitance for hMO_x-RuO_2 and commercial RuO_2 supported on carbon (a) and carbon nanotubes (b) at different current densities; comparison of the long-term cycling performance of hMO_x-RuO_2 and commercial RuO_2 supported on carbon (c) and carbon nanotubes (d) at current density of 1 A g^{-1}; comparison of Nyquist plots for hMO_x-RuO_2 and commercial RuO_2 supported on carbon (e) and carbon nanotubes (f).

tial capacitances, other hMO_x-RuO_2/C and hMO_x-RuO_2/CNT electrode materials exhibit excellent stability with at least 91.2% retention of the initial capacitance (hFe_2O_3-RuO_2/C). These retention ratios at constant current density are comparable and even better than those of the commercial RuO_2 supported on carbon (94.5%) or carbon nanotubes (97.2%). In particular, the specific capacitance retention ratios after 5000 cycles for hCoO-RuO_2/C, hCoO-RuO_2/CNT, hNiO-RuO_2/C, and hNiO-RuO_2/CNT were also tested, which are 93.9%, 94.1%, 88.0% and 89.8%, respectively, as exhibited by Fig. S6. The high cycling stability might have also benefited from the hollow interiors of the binary or ternary metal oxides, which could alleviate the strain effect developed during the frequent charge-discharge process.

The specific power density (P) and energy density (E) were calculated using the following equations:

$$P = V^2 / 4mR, \quad (2)$$

$$E = CV^2/2, \quad (3)$$

where P and E are the specific power density (kW kg^{-1}) and energy density (W h kg^{-1}), respectively, V is the maximum potential (V), R is the equivalent series resistance (Ω), m is the mass of the electro-active materials in the capacitor (g), and C is the specific capacitance (F g^{-1}). As listed in Table S5, in this work, the equivalent series resistances of the capacitors based on hCoO-RuO_2/C, hCoO-RuO_2/CNT, hCuO-RuO_2/C, hCuO-RuO_2/CNT, hFe_2O_3-RuO_2/C, hFe_2O_3-RuO_2/CNT, hNiO-RuO_2/C, hNiO-RuO_2/CNT, $hCu_{0.6}Ni_{0.4}O$-RuO_2/C, $hCu_{0.6}Ni_{0.4}O$-RuO_2/CNT, commercial RuO_2/C, and commercial RuO_2/CNT are 2.37, 1.26, 3.27, 1.07, 2.18, 1.97, 1.03, 0.68, 2.54, 1.55, 1.19, and 1.01 Ω, respectively. Calculations by the Equations (2 and 3) above indicate that the specific power densities (P) for the capacitor based on hCoO-RuO_2/C, hCoO-RuO_2/CNT, hCuO-RuO_2/C, hCuO-RuO_2/CNT, hFe_2O_3-RuO_2/C, hFe_2O_3-RuO_2/CNT, hNiO-RuO_2/C, hNiO-RuO_2/CNT, $hCu_{0.6}Ni_{0.4}O$-RuO_2/C, $hCu_{0.6}Ni_{0.4}O$-RuO_2/CNT, commercial RuO_2/C, and commercial RuO_2/CNT are 38.0, 71.4, 27.5, 84.1, 41.3, 45.7, 87.4, 132.4, 35.4, 58.1, 75.6, and 90.0 W kg^{-1}, respectively, while the energy densities (E) are 129.8, 128.4, 136.2, 136.4, 119.0, 106.2, 151.8, 158.4, 125.9, 128.8, 144.3, and 145.9 Wh kg^{-1}, respectively, which are also placed in Table S5. Notably, there are two features could be observed from Table S5: the samples supported on carbon nanotubes have lower series resistances than those of the same supported on carbon substrates; the hNiO-RuO_2/CNT has the lowest series resistance among all electrode materials. Therefore, the supercapacitor based on hNiO-RuO_2/CNT has the highest power and energy densities, which are 132.4 W kg^{-1} and 158.4 Wh kg^{-1}, respectively, essentially in keeping with its high specific capacitance.

Figs 6e and f show the Nyquist plots of the hMO_x-RuO_2 and commercial RuO_2 supported on carbon and carbon nanotubes, respectively, measured by EIS, which illustrate the frequency response of the electrode/electrolyte system. In the low-frequency area, the line slope in the EIS plots indicates Warburg impedance, which is caused by ionic diffusion, and could be governed by the physical characters of the electrode materials, e.g., particle size, specific surface area, and diffusion distance. The more vertical the curve, the more closely the supercapacitor behaves as an ideal capacitor. As shown in the Nyquist plots, in the low-frequency area the curves of the hCoO-RuO_2/C and hNiO-RuO_2/C (Fig. 6e) as well as the hCoO-RuO_2/CNT and hNiO-RuO_2/CNT (Fig. 6f) are more vertical to the x axis than those of other carbon or carbon nanotube-supported hollow oxides and commercial RuO_2, indicating a significant enhancement of the charge transport in hCoO-RuO_2/C, hNiO-RuO_2/C, hCoO-RuO_2/CNT, and hNiO-RuO_2/CNT electrodes. In the high-frequency area, the interception of the curve in the real part Z' indicates the bulk resistance of the electrochemical system. Obviously, the hNiO-RuO_2/C and hNio-RuO_2/CNT electrodes display very low bulk resistance.

Finally, as a vivid demonstration of the application of these hollow structured binary or ternary metal oxides, we fabricated three symmetric cells, which were consisted of hCoO-RuO_2/C, hCuO-RuO_2/C, and hNiO-RuO_2/C electrodes, respectively. These cells were charged at a constant voltage of 1.2 V for 5 min, and then were connected in series to run a white light emitting diode (LED, 5 mm, 3.0 V, 30 mA), as illustrated in Fig. S7. We noticed that the LED remains very bright even after 30 min of operation, manifesting application potentials of these hollow binary or ternary Ru-based oxides in practical supercapacitors.

CONCLUSION

In summary, we reported a general approach based on the combination of the galvanic replacement process with a subsequent thermal treatment to produce carbon or carbon nanotube-supported hollow nanostructures of Ru-based binary or ternary oxides as highly efficient electrodes for supercapacitors. This strategy involves the synthesis of the transition metal nanoparticles including Co, Cu, Fe, Ni, or CuNi, and subsequent replacement reaction with Ru ion precursors for the preparation of binary or ternary hollow

nanostructures composed of corresponding transition metal and Ru, which are then loaded on carbon or carbon nanotube substrates and subjected to a thermal treatment in air to generate binary or ternary Ru-based metal oxides with hollow interiors. The as-prepared Ru-based hollow oxides show superior performance as electrodes for a supercapacitor. Specifically, the binary hollow nanostructures composed of NiO and RuO_2 supported on carbon nanotubes with RuO_2 mass ratio of 19.6% exhibit high specific capacitances of 740.0 F g^{-1} with good cycle stability at a current density of 1 A g^{-1} in a symmetric capacitor adopting KOH as electrolyte, much higher than that of commercial RuO_2 supported on the same substrates (620.1 F g^{-1}). The hollow interiors formed during the galvanic replacement process not only enhance the electro-active sites by increasing the specific surface area of RuO_2-based binary and ternary electrodes, but also facilitate the charge transport in the electro-active materials by shortening the diffusion distance. The concept used to fabricate hollow structured binary or ternary Ru-based oxides might be extended to produce other multiple metal oxides as highly efficient electrode materials for a supercapacitor.

Received 26 April 2016; accepted 20 May 2016; published online 30 May 2016

1 Zhao DD, Bao SJ, Zhou WH, *et al.* Preparation of hexagonal nanoporous nickel hydroxide film and its application for electrochemical capacitor. Electrochem Commun, 2007, 9: 869–874
2 Patake VD, Lokhande CD, Joo OS. Electrodeposited ruthenium oxide thin films for supercapacitor: effect of surface treatments. Appl Surf Sci, 2009, 255: 4192–4196
3 Brezesinski T, Wang J, Tolbert SH, *et al.* Ordered mesoporous α-MoO_3 with iso-oriented nanocrystalline walls for thin-film pseudocapacitors. Nat Mater, 2010, 9: 146–151
4 Wu Q, Xu Y, Yao Z, *et al.* Supercapacitors based on flexible graphene/polyaniline nanofiber composite films. ACS Nano, 2010, 4: 1963–1970
5 Wang K, Huang J, Wei Z. Conducting polyaniline nanowire arrays for high performance supercapacitors. J Phys Chem C, 2010, 114: 8062–8067
6 Lang X, Hirata A, Fujita T, *et al.* Nanoporous metal/oxide hybrid electrodes for electrochemical supercapacitors. Nat Nanotechnol, 2011, 6: 232–236
7 Yan D, Guo Z, Zhu G, *et al.* MnO_2 film with three-dimensional structure prepared by hydrothermal process for supercapacitor. J Power Sources, 2012, 199: 409–412
8 Simon P, Gogotsi Y. Materials for electrochemical capacitors. Nat Mater, 2008, 7: 845–854
9 Wang G, Zhang L, Zhang J. A review of electrode materials for electrochemical supercapacitors. Chem Soc Rev, 2012, 41: 797–828
10 Liu S, Sun S, You XZ. Inorganic nanostructured materials for high performance electrochemical supercapacitors. Nanoscale, 2014, 6: 2037–2045
11 Soin N, Roy SS, Mitra SK, *et al.* Nanocrystalline ruthenium oxide dispersed few layered graphene (FLG) nanoflakes as supercapacitor electrodes. J Mater Chem, 2012, 22: 14944–14950
12 Chen LY, Hou Y, Kang JL, *et al.* Toward the theoretical capacitance of RuO_2 reinforced by highly conductive nanoporous gold. Adv Energy Mater, 2013, 3: 851–856
13 Ananth A, Dharaneedharan S, Gandhi MS, *et al.* Novel RuO_2 nanosheets-facile synthesis, characterization and application. Chem Eng J, 2013, 223: 729–736
14 Kim JY, Kim KH, Kim HK, *et al.* Nanosheet-assembled 3D nanoflowers of ruthenium oxide with superior rate performance for supercapacitor applications. RSC Adv, 2014, 4: 16115–16120
15 Pico F, Ibañez J, Lillo-Rodenas MA, *et al.* Understanding RuO_2·xH_2O/carbon nanofibre composites as supercapacitor electrodes. J Power Sources, 2008, 176: 417–425
16 Wu ZS, Wang DW, Ren W, *et al.* Anchoring hydrous RuO_2 on graphene sheets for high-performance electrochemical capacitors. Adv Funct Mater, 2010, 20: 3595–3602
17 Zhang J, Jiang J, Li H, *et al.* A high-performance asymmetric supercapacitor fabricated with graphene-based electrodes. Energy Environ Sci, 2011, 4: 4009–4015
18 Fang HT, Liu M, Wang DW, *et al.* Fabrication and supercapacitive properties of a thick electrode of carbon nanotube-RuO_2 core-shell hybrid material with a high RuO_2 loading. Nano Energy, 2013, 2: 1232–1241
19 Zhou Z, Zhu Y, Wu Z, *et al.* Amorphous RuO_2 coated on carbon spheres as excellent electrode materials for supercapacitors. RSC Adv, 2014, 4: 6927–6932
20 Kim H, Popov BN. Characterization of hydrous ruthenium oxide/carbon nanocomposite supercapacitors prepared by a colloidal method. J Power Sources, 2002, 104: 52–61
21 Pico F, Morales E, Fernandez JA, *et al.* Ruthenium oxide/carbon composites with microporous or mesoporous carbon as support and prepared by two procedures. A comparative study as supercapacitor electrodes. Electrochim Acta, 2009, 54: 2239–2245
22 Liu Y, Zhao W, Zhang X. Soft template synthesis of mesoporous Co_3O_4/RuO_2·xH_2O composites for electrochemical capacitors. Electrochim Acta, 2008, 53: 3296–3304
23 Hyun TS, Kang JE, Kim HG, *et al.* Electrochemical properties of MnO_x–RuO_2 nanofiber mats synthesized by co-electrospinning. Electrochem Solid-Sate Lett, 2009, 12: A225–A228
24 Lee JB, Jeong SY, Moon WJ, *et al.* Preparation and characterization of electro-spun RuO_2–Ag_2O composite nanowires for electrochemical capacitors. J Alloy Compd, 2011, 509: 4336–4340
25 Xu J, Wang Q, Wang X, *et al.* Flexible asymmetric supercapacitors based upon Co_9S_8 nanorod/Co_3O_4@RuO_2 nanosheet arrays on carbon cloth. ACS Nano, 2013, 7: 5453–5462
26 Rakhi RB, Chen W, Hedhili MN, *et al.* Enhanced rate performance of mesoporous Co_3O_4 nanosheet supercapacitor electrodes by hydrous RuO_2 nanoparticle decoration. ACS Appl Mater Interfaces, 2014, 6: 4196–4206
27 Ghosh A, Lee YH. Carbon-based electrochemical capacitors. ChemSusChem, 2012, 5: 480–499
28 Zhi M, Xiang C, Li J, *et al.* Nanostructured carbon–metal oxide composite electrodes for supercapacitors: a review. Nanoscale, 2013, 5: 72–88
29 Liu X, Atwater M, Wang J, *et al.* A study on gold nanoparticle synthesis using oleylamine as both reducing agent and protecting ligand. J Nanosci Nanotechnol, 2007, 7: 3126–3133
30 Xu Z, Shen C, Hou Y, *et al.* Oleylamine as both reducing agent and stabilizer in a facile synthesis of magnetite nanoparticles. Chem Mater, 2009, 21: 1778–1780
31 Stefanos M, Liz-Marzan LM. Oleylamine in nanoparticle synthesis. Chem Mater, 2013, 25: 1465–1476

32 Moulder JF, Chastain J. Handbook of X-ray Photoelectron Spectroscopy. A Reference Book of Standard Spectra for Identification and Interpretation of XPS Data. Eden Prairie Minnesota: Physical Electronics Division Perkin-Elmer Corp, 1992
33 Powell CJ. Recommended Auger parameters for 42 elemental solids. J Electron Spectrosc Relat Phenom, 2012, 185: 1–3
34 Conner GR. Combination analysis of metal oxides using ESCA, AES, and SIMS. J Vac Sci Technol, 1978, 15: 343–347
35 Tan BJ, Klabunde KJ, Sherwood PMA. XPS studies of solvated metal atom dispersed catalysts. Evidence for layered cobalt-manganese particles on alumina and silica. J Am Chem Soc, 1991, 113: 855–861
36 Sun Y, Xia Y. Alloying and dealloying processes involved in the preparation of metal nanoshells through a galvanic replacement reaction. Nano Lett, 2003, 3: 1569–1572
37 Chen HM, Liu RS, Lo MY, *et al.* Hollow platinum spheres with nanochannels: synthesis and enhanced catalysis for oxygen reduction. J Phys Chem C, 2008, 112: 7522–7526
38 Ye F, Liu H, Hu W, *et al.* Heterogeneous Au–Pt nanostructures with enhanced catalytic activity toward oxygen reduction. Dalton Trans, 2012, 41: 2898–2903
39 Liu Z, Lee JY, Han M, *et al.* Synthesis and characterization of PtRu/C catalysts from microemulsions and emulsions. J Mater Chem, 2002, 12: 2453–2458
40 Zhang X, Chen KY. Water-in-oil microemulsion synthesis of platinum-ruthenium nanoparticles, their characterization and electrocatalytic properties. Chem Mater, 2003, 15: 451–459
41 Ye F, Liu H, Yang JH, *et al.* Morphology and structure controlled synthesis of ruthenium nanoparticles in oleylamine. Dalton Trans, 2013, 42: 12309–12316
42 Kishi K, Sasanuma M. The interaction of O_2 with Cu/Ni(100) and Cu/NiO/Ni(100) surfaces studied by XPS. J Electron Spectrosc Relat Phenom, 1989, 48: 421–434
43 Kim BC, Wallace GG, Yoon YI, *et al.* Capacitive properties of RuO_2 and Ru-Co mixed oxide deposited on single-walled carbon nanotubes for high-performance supercapacitors. Synthetic Mat, 2009, 159: 1389–1392
44 Pusawale SN, Deshmukh PR, Gunjakar JL, *et al.* SnO_2-RuO_2 composite films by chemical deposition for supercapacitor application. Mater Chem Phys, 2013, 139: 416–422

Acknowledgments This work was supported by the National Natural Science Foundation of China (21173226, 21376247, 21573240 and 21506225), Center for Mesoscience, Institute of Process Engineering, Chinese Academy of Sciences (COM2015A001), and the Knowledge Innovation Program of the Chinese Academy of Sciences (KGCX2-YW-341).

Author contributions Tan Q, Wang P, Liu H and Xu Y performed the materials synthesis, characterization and electrochemical measurements. Chen Y was involved in data analysis and discussion. Yang J conceived the strategy, supervised the design of experiments, and wrote the manuscript, and all authors participated in the review of the manuscript.

Conflict of interest The authors declare that they have no conflict of interest.

Supplementary information Experimental details are available in the online version of the paper.

Qiangqiang Tan received his PhD degree in physical chemistry of metallurgy at the University of Science and Technology Beijing in 2003. After two years of postdoctoral research at the Institute of Electrical Engineering, Chinese Academy of Sciences (IPE-CAS), he joined the State Key Laboratory of Multi-phase Complex System, IPE-CAS, as an associate professor, and was then promoted to be a full professor. His research interest focuses on novel materials for energy conversion and storage, novel ceramics materials, and comprehensive utilization of ore resources.

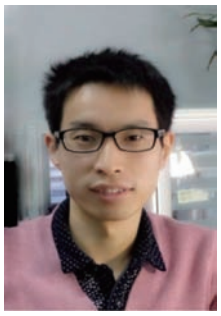

Pengfei Wang received his BSc degree in chemical engineering and processing at Harbin Engineering University in 2012. He is currently a PhD student at the Institute of Process Engineering, Chinese Academy of Sciences (IPE-CAS). His research focuses on the metal oxide-based nanocomposites as highly efficient electrode materials for supercapacitors.

Jun Yang received his PhD degree in chemical and biomolecular engineering in 2006 from National University of Singapore. After postdoctoral research at Boston College and University of Toronto, he joined the Institute of Bioengineering and Nanotechnology, Singapore in 2007. In 2010, he moved to the Institute of Process Engineering, Chinese Academy of Sciences as the group leader of Materials for Energy Conversion and Environmental Remediation (MECER). His main research interests include applied catalysis, nanocomposites for energy conversion, synthesis and application of novel nanocrystalline materials, and separation techniques.

中空MO_x-RuO_2纳米结构用作高效超级电容器电极材料

谭强强[1], 王鹏飞[1,2], 刘卉[1,3], 徐宇兴[1], 陈运法[1], 杨军[1,3*]

摘要 以低成本的方式调控纳米材料的内部结构和化学成分对增强其在特定应用中的性能非常重要, 但挑战巨大. 本文将电置换反应与一种热处理过程相结合, 报道了一种具有普适性的途径制备钌基二元和三元氧化物纳米中空结构, 并测定了其作为超级电容器电极材料的性能. 结果表明, 采用KOH为电解质, 在RuO_2的质量分数仅为19.6%时, 所获得的负载于碳纳米管表面的中空NiO-RuO_2纳米结构在恒电流密度为1 A g^{-1}时具有740 F g^{-1}的比容量, 并且具有良好的循环稳定性. 在恒电流密度为5 A g^{-1}时, 比容量仍可以保持在638.4 F g^{-1}. 本文以RuO_2提高过渡金属的导电性, 以过渡金属降低RuO_2材料成本并结合中空结构增加材料表面积的思路, 可以借鉴用来制备其它金属氧化物体系以满足特定应用的需求.